ENGINEERING

Charting the envelope of mechanical properties of synthetic silk fibers through predictive modeling of the drawing process

Jacob J. Graham[1], Shri V. Subramani[2], Xinyan Yang[3], Timothy M. Russell[1], Fuzhong Zhang[2], Sinan Keten[1,3]*

A major challenge in synthesizing strong and tough protein fibers based on spider silk motifs is understanding the coupling between protein sequence and the postspin drawing process. We clarify how drawing-induced elongational force affects ordering, chain extension, interchain contacts, and molecular mobility through mesoscale simulations of silk-based fibers. We show that these emergent features can be used to predict mechanical property enhancements arising from postspin drawing. Simulations recapitulate a purely process-dependent mechanical property envelope in which order enhances fiber strength while preserving toughness. The relationship between chain extension and crystalline domain alignment observed in simulations is validated by Raman spectroscopy of wet-spun fibers. Property enhancements attributed to the progression of anisotropic extension are verified by mechanical tests of drawn silk fibers and justified by theory. These findings elucidate how drawing enhances properties of protein-based fibers and shed light on how to incorporate this effect into predictive models.

INTRODUCTION

Protein-based materials like silk are gaining broad appeal for their exceptional and tunable mechanical properties. Natural spider silk fibers exhibit tensile strength in the same range as steel with toughness achieved through rubber-like extension rivaling that of Nylon and Kevlar fabrics (*1*, *2*). Although it cannot yet fully replicate the remarkable mechanical properties of its native counterpart (*3*), synthetic silk fiber produced by the recombinant approach is still strong (*4*), tough, elastic, biodegradable (*5*), biocompatible (*6*), and antimicrobial (*7*). These properties shared with natural silk have inspired the design of sutures (*8*), protein-based adhesives (*9*), vascular grafts (*10*), metabolite monitoring biosensors (*11*), and other tissue engineering applications (*12*). Insurmountable challenges prohibit scalable spider silk farming to the extent that complete natural spider silk garments have only ever been made for exhibition at great effort and cost (*13*). Furthermore, recombinant synthesis enables researchers to expand the library of sequence-property relationships beyond those fibers found in nature documented in the recently released Spider Silkome Database (*14*). Such precise control of primary amino acid sequence has stimulated a research field dedicated to manipulating the properties of wet-spun protein-based fibers (*15*, *16*) through consensus sequencing (*17*, *18*), domain fusion (*4*, *19*, *20*), directed evolution, secondary structure design principles (*21*, *22*), and machine learning approaches (*23*). However, fiber mechanical properties by no means depend exclusively on sequence. Peptide assembly in the silk gland is a multistage process by which micellar (*24*) aggregates are disrupted by pH gradients and shear flow along the tapered duct (*25*) before assembling into a matrix of β crystals embedded in an amorphous matrix (*26*). Understanding how peptide conformational changes drive assembly during this process is therefore necessary to develop biomimetic spinning approaches yielding fibers with predictable mechanical properties.

In the past, computational modeling strategies targeting silk protein dynamics have confirmed theories of shear-induced crystal formation and network percolation (*27*, *28*) and the effects of sequence features and hydrodynamic flow on silk assembly (*29*, *30*). It has also been shown that terminal domain interactions in shear flow enhance the order of those extended domains tethering aggregates together (*31*). These studies all reveal the critical role that anisotropy plays in the mechanics of silk fibers but do not directly correlate molecular descriptors of anisotropy with fiber mechanical properties. In this work, we use a coarse-grained dissipative particle dynamics (DPD) representation of silk as a simple diblock copolymer (*27*–*29*, *31*) in solvent to capture mechanical property trends as they relate to protein orientation and extension arising from postspin drawing. At a molecular scale, the degree of anisotropy of individual proteins can be quantified by their shape and orientation relative to the fiber axis. End-to-end length and Hermans order parameter, when considered together, quantify the degree of anisotropy in a bulk protein or polymer matrix. At the same time, the greater end-to-end length of individual proteins promotes formation of stable hydrogen bonds perpendicular to the fiber axis, which can enhance strength and toughness while decreasing fiber extensibility. By extending proteins along the fiber axis directly before uniaxial tensile tests, we demonstrate how order, elongation, and interprotein hydrogen bonding are responsible for the modular toughness, elastic modulus, maximum stress, and maximum strain achieved through postspin drawing. To control the molecular order and alignment of individual proteins in simulations, an equal and opposite pull force is applied to the two ends of each protein during processing. We find substantial variability in the degree to which this pull force increases protein end-to-end length and Hermans order parameter for proteins of differing molecular weight (MW). While higher-MW proteins have greater extensibility at low forces, they require higher forces to achieve the same degree of order as shorter proteins. We also derive correlations

---

[1]Department of Mechanical Engineering, Northwestern University, Evanston, IL 60208, USA. [2]Department of Energy, Environmental & Chemical Engineering, Washington University in St. Louis, St. Louis, MO 63130, USA. [3]Department of Civil and Environmental Engineering, Northwestern University, Evanston, IL 60208, USA.
*Corresponding author. Email: s-keten@northwestern.edu

between order, hydrogen bond counts, and mean squared displacement (MSD), features that have been emphasized in previous theoretical descriptions of the silk property envelope (*23*, *32*–*34*). Last, we link these features to the wide ranging mechanical properties observed through drawing in both simulated and recombinant silk fibers and discuss their role in energy storage for property enhancement. Our work reveals the process dependence of molecular-level features on structure and mechanical properties, which is an important step toward developing hybrid computational, experimental, and theoretical predictive models that consider the process as much as the composition of polymer materials.

RESULTS

Pull force–induced molecular order and alignment

The force field parameters for the hydrophilic, hydrophobic, and water beads in this study were derived and validated in a previous work (*27*) to reflect the consensus sequence of major ampullate spidroin (MaSp1) of *Nephila clavipes* (*35*, *36*). Repulsive interaction parameters between beads of the same species were chosen to match the compressibility of water (*37*), while the repulsive parameters between domains of “a”- and “b”-type beads were rationalized by their ability to qualitatively capture diblock copolymer behavior such as micelle formation in the equilibrium state (*37*, *38*). In this study, three distinct MWs are simulated in equal concentrations of 20% (w/v). This concentration is common for the viscous dopes used for high-MW synthetic silk extrusion but is much lower than that of natural dope, which can reach concentrations of up to 50% (w/v) (*39*). Proteins consisting of 2, 8, and 16 repeats of the alternating hydrophilic/hydrophobic spider silk motif, referred to here on as $n = 2$, $n = 8$, and $n = 16$, are represented by linear chains of beads connected by harmonic springs. The $n = 16$ proteins are used as a basis for comparing simulated mechanical property and molecular alignment results to fibers wet spun from a synthetic silk-amyloid hybrid copolymer. Three amino acids are mapped to one coarse-grained bead for proteins, and nine water molecules are modeled using a single water bead. Each motif contains seven “b”-type beads per hydrophilic domain followed by five “a”-type beads per hydrophobic domain. In Fig. 1, “b”-type hydrophilic beads are depicted in blue with the “a”-type beads depicted in red. A tail of three hydrophilic particles representing a decahistidine tag, used to purify recombinant synthetic silk peptides through immobilized metal affinity chromatography, is added to the end of each simulated protein modeled with hydrophobic “b”-type beads. More details regarding interaction parameters of the coarse-grained model can be found in Supplementary Text.

Silk drawing is a critical step in both natural and synthetic silk spinning (*40*). Drawing forces in synthetic silk spinning are applied through forced reeling (*41*) or by immersing as-spun fibers back into the extrusion bath and manually stretching the fiber to a desired draw ratio (λ_{draw}) (*42*–*44*). To emulate protein extension and

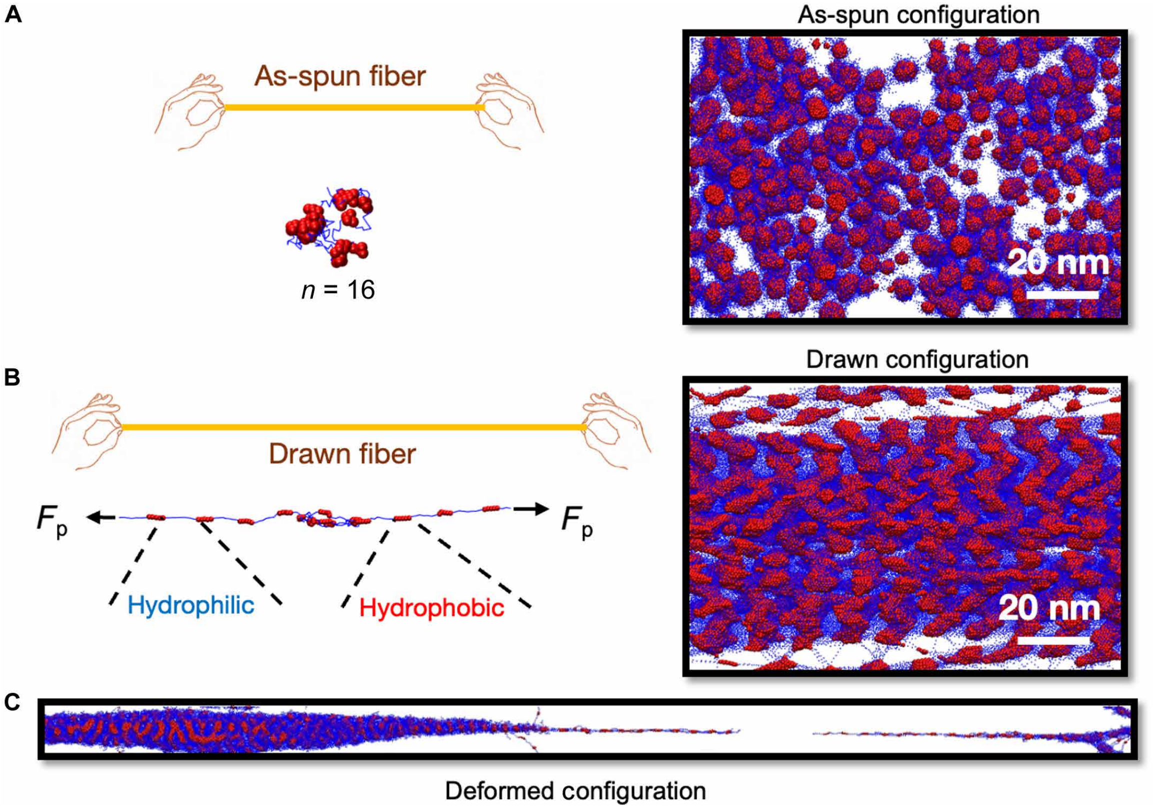

Fig. 1. Summary of the computational protocol for mimicking drawn silk fibers. (**A**) Snapshots of a single 16-repeat simulated silk protein in the undrawn state and DPD simulations of as-spun silk systems. (**B**) Snapshots of a single 16-repeat silk protein in the drawn state achieved through pull force (F_p) applied to the left and right ends of the protein and DPD simulations of drawn silk systems. (**C**) Last, a high-frequency deformation is performed to stretch the drawn fibers to failure and measure their relative mechanical properties.

alignment during manual postspin drawing, an equal and opposite pull force (F_p) is applied to the ends of each chain after an initial equilibration of the system. An appropriate bond-breaking criterion has not been established for this model, so we use only processing pull forces that would consistently unravel but not rupture individual proteins. According to previous atomic force microscopy (AFM) studies of 16-repeat synthetic silk peptides inspired by *N. clavipes*, pull forces on individual proteins beyond 220 pN cause the protein to unravel from its β sheet–rich secondary structure (*45*). While the drawing process likely causes some rupture of individual proteins, this model can only capture changes because of realignment and reassembly after shear flow from extrusion and not bond breaking. The processing pull force is therefore limited to 222 pN. The system processed with no pull force equilibrium molecular dynamics is referred to as the as-spun configuration in Fig. 1. For a discussion on how the equilibration step affects final fiber properties, see the "Impact of Equilibration on Properties and Molecular Features" section in the Supplementary Materials. Figure 1 summarizes how application of F_p visually changes the conformation of individual chains and the protein assembly. Extension of a single simulated $n = 16$ protein, depicted in Fig. 1B, imitates the hypothetical change that a single silk-amyloid protein undergoes during the drawing process, resulting in enhanced β strand alignment.

Starting from an initial configuration of random walk chains and randomly placed water beads, the entire end-to-end simulation protocol begins with an equilibration step during which peptides aggregate into micellar structures like those shown in Fig. 1A. Following this equilibration, a pull force processing step is performed during which a prescribed value of F_p is used to extend proteins along what eventually becomes the axis of deformation under uniaxial tension (Fig. 1B). The pull force is then released, during which features of interest are monitored for changes, before running a uniaxial tensile deformation to characterize mechanical properties (Fig. 1C). The purpose of the pull force during processing is to induce order and extension, which are measured using Hermans order parameter (s) and end-to-end length (R_{ee}), respectively. These quantitative descriptions of alignment and degree of extension in simulations are ultimately compared to experimentally derived metrics of β sheet alignment and drawing ratio. Figure 2 (A and B) summarizes how variables s and R_{ee} change throughout the equilibration, processing, relaxation, and tensile tests for the $n = 16$–repeat protein, confirming that s and R_{ee} are sensitive to F_p not only during pull processing but also during the resulting tensile deformation. Figures S1 and S2 summarize how s and R_{ee} change from the initial configuration through tensile deformation for the $n = 2$ and $n = 8$ proteins. In some cases of low F_p and low MW, we observed a drop in s to its initial value during relaxation such that order values were indistinguishable between these systems at the end of that step. For example, in Fig. 2B, after applying $F_p = 22.2$ pN, s decreases to ~0. However, distinct differences in the behavior of s and R_{ee} during the deformation step were still observed between $F_p = 22.2$ pN and the as-spun case with $F_p = 0$ pN during processing. Because of this, variables s_0 and R_{ee} introduced in Fig. 2 (A and B) refer to the average order parameter as calculated at the end of the pull processing step. These values will be the property of interest when comparing mechanical properties and molecular features rather than order after the postrelaxation step throughout this paper. A detailed description of conversion between the dimensionless unit convention of DPD simulations and real units is provided in Supplementary Materials and Methods.

Figure 2 (C and D) confirms that while longer proteins are more extensible under the influence of F_p, much larger force is required to achieve the same level of order at the end of the processing step. This processing method does not give us independent control over s_0 and R_{ee}, so we define two variables in Fig. 2 (C and D), contour length–normalized end-to-end length ($R_{ee}/N_m b$) and extension ratio (λ_{ee}), which describe both the degree of extension and how it relates to s_0 for different MWs. By normalizing R_{ee} by the protein contour length, which is equal to the number of monomers (N_m) multiplied by the equilibrium bond length between beads (b), we can see that low-MW systems readily achieve very high degree of order with increasing force and that $R_{ee}/N_m b$ is higher for low-MW systems (Fig. 2E). On the other hand, λ_{ee}, which is the ratio of R_{ee} at the end of processing to R_{ee} in the as-spun configuration, indicates that this quantity is more sensitive to force in higher-MW proteins and attains a higher value at any given degree of order.

Effect of molecular order on hydrogen bonding and MSD

Strain-induced crystallization driven by the zipper-like hydrogen bonds that can form between aligned β strand–forming domains has been observed in many polymeric materials (*46*). In both natural and synthetic spider silk, faster silk reeling speeds increase crystallinity and produce stiffer fibers (*41*, *47*–*49*). In the original conceptualization of this model of coarse-grained silk, an additional nonbonded harmonic potential term is added between "a"-type beads to capture the increased propensity for hydrogen bonds to form between these domains. A hydrogen bond is defined here as any instance in which two "a"-type beads are within the cutoff distance of interaction for the hydrogen bond potential energy function, which is equal to the model's characteristic length $R_c = 9.321$ Å. A detailed description of the hydrogen bond potential is provided in Supplementary Materials and Methods.

To understand how s_0 influences hydrogen bonding in the DPD model of drawn silk, we counted the total number of hydrogen bonds that were forming in the system (HB^{tot}) and normalized it by the number of hydrogen bonds that formed in the as-spun fiber (HB_{as}), showing that for all MWs studied, there is a moderate increase in overall hydrogen bonding between ~3 and 8% (Fig. 3A). This is consistent with the results of wide-angle x-ray scattering experiments of wet-spun silk fibers collected in previous work, whereby ~10% crystallinity increases were observed with a postspin draw ratio of 7 (*48*). However, interprotein connectivity has been described as playing a substantial role in enhancing mechanical properties of synthetic silk (*28*), so we also measured the number of interprotein hydrogen bonds that formed (HB^{inter}), finding that such bonds made up an increasing proportion of HB^{tot} with increasing s_0 (Fig. 3B). Notably, the proportion of HB^{inter}/HB^{tot} reported in Fig. 3B decreased with MW in the as-spun state, suggesting that as MW increases, a disproportionate number of hydrogen bonds form within rather than between proteins when there is no drawing force. Figure 3C shows that the percent change in proportion HB^{inter}/HB^{tot} versus HB^{inter}/HB^{tot} when $s_0 = 0$ ($\Delta HB^{inter}/HB^{tot}$ %) increases the fastest in the $n = 16$ proteins, emphasizing the importance of processing-induced order and extension in enhancing interprotein hydrogen bonding for high-MW proteins. Snapshots of systems with varying degrees of order taken at the end of the pull processing step show the transition of micellar structures to structures resembling lamella (Fig. 3D), which form when separate domains extend and stack onto each other. This transition is the most likely explanation for the

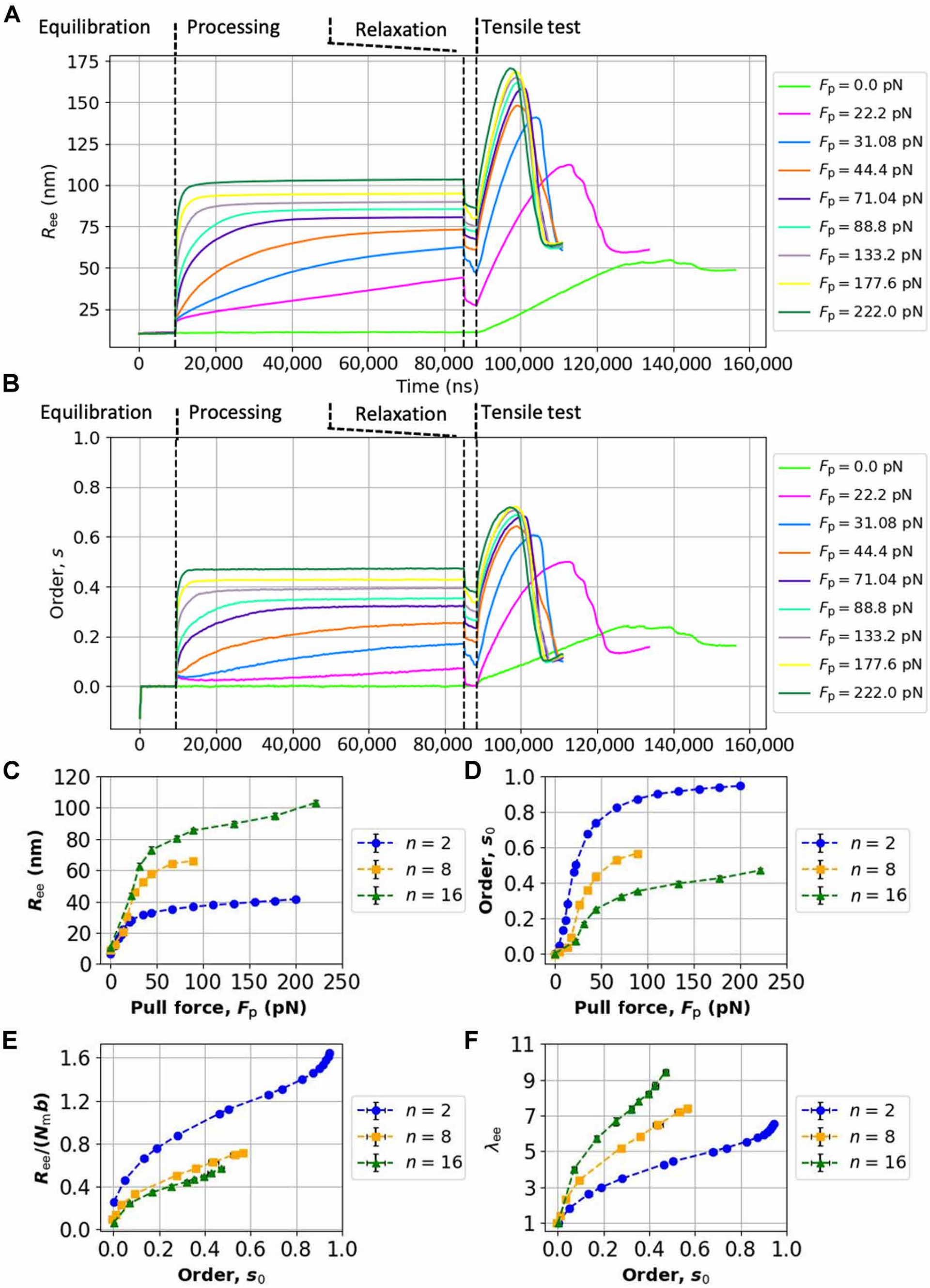

Fig. 2. Effect of F_p on order and extension. (**A**) End-to-end length (R_{ee}) of $n = 16$ proteins plotted as a function time through all steps of simulation. (**B**) Hermans order parameter (s) of $n = 16$ proteins plotted as a function of time through all steps of simulation. (**C**) End-to-end lengths of simulated silk peptides were quantified as a function of F_p at the end of the processing step, just before F_p was released. (**D**) Average s_0 was also calculated at the end of the processing step to tune which pull forces are required to induce chain order. (**E**) The ratio of end-to-end length of each chain is normalized by dividing R_{ee} by the contour length ($N_m b$). (**F**) s_0 is then compared to the ratio of final to initial average chain length (λ_{ee}) for the three protein sizes tested.

increase in interprotein hydrogen bonding density at high s_0 and MW. By tracking hydrogen bond counts through simulated tensile tests, we demonstrated in fig. S3 that fibers processed to have a greater number and proportion of interprotein hydrogen bonds also achieve greater hydrogen bonding throughout the deformation. In addition, we measured how total hydrogen bonding initially decreases in the elastic region in fig. S4A but stabilizes in the postyield strain hardening region. For more details on time and spatial analysis of hydrogen bonds through simulated tensile tests, see figs. S3 and S4 in the "Hydrogen Bond Trends Through Simulated Tensile Tests" section in the Supplementary Materials.

MSD, known also as Debye-Waller factor or *B*-factor in the context of proteins, is a short timescale measure of local stiffness coming from thermal vibrations of particles (*50*–*52*). It is another metric

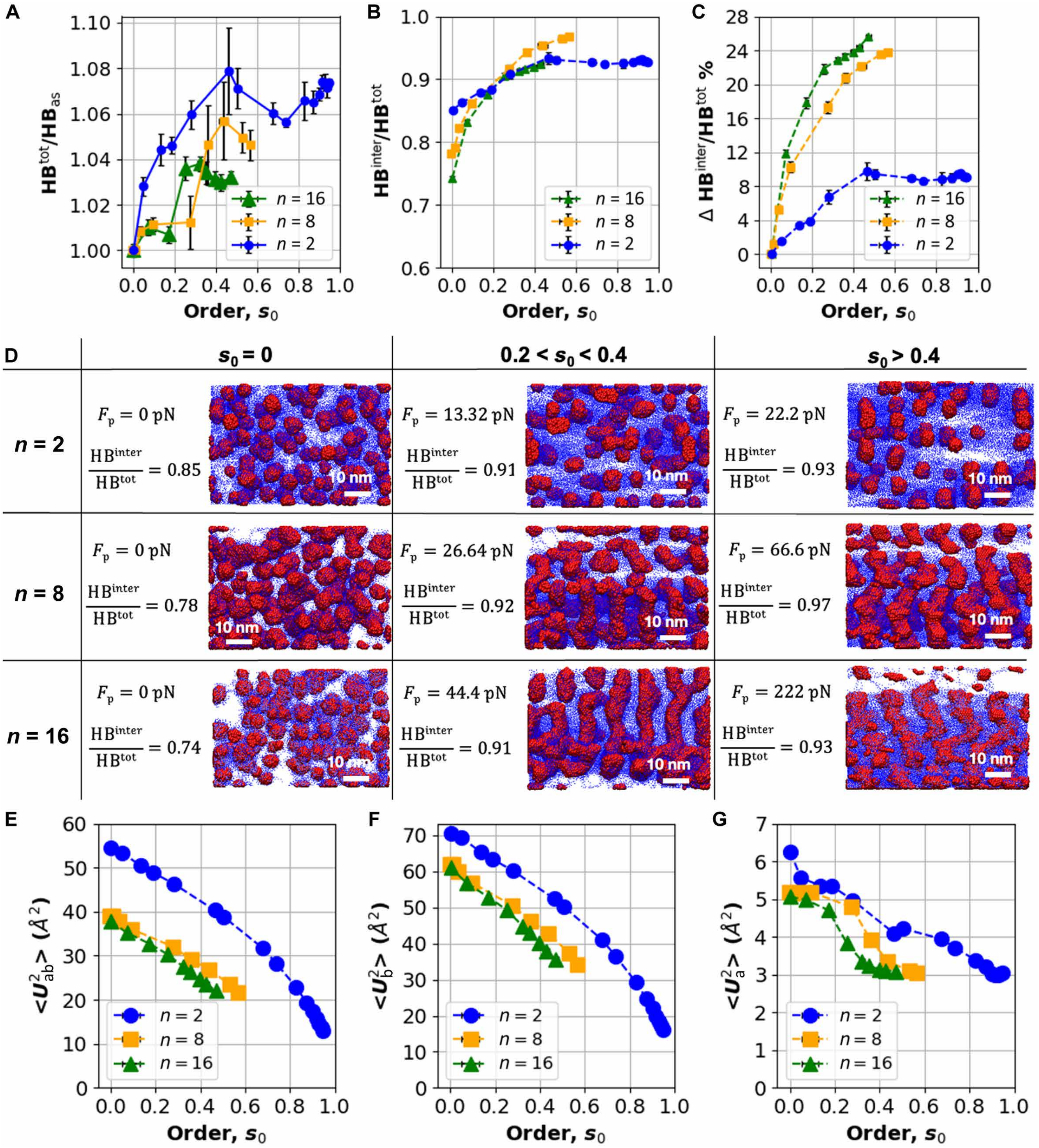

Fig. 3. Effects of s_0 on hydrogen bonding and MSD. (**A**) Ratio of the number of hydrogen bonds in the ordered configuration (HB^{tot}) versus the number of hydrogen bonds in the as-spun configuration (HB_{as}) for simulated $n = 2$, $n = 8$, and $n = 16$ proteins. (**B**) Ratio of interprotein hydrogen bonds (HB^{inter}) to total hydrogen bonds (HB^{tot}) plotted as a function of s_0. (**C**) Percent change in the ratio of HB^{inter}/HB^{tot} versus HB^{inter}/HB^{tot} ($\Delta HB^{inter}/HB^{tot}$ %) relative to the as-spun case of $s_0 = 0$. (**D**) Snapshots of simulations for all three MWs simulated at the end of the pull force processing step. Examples of low ($s_0 = 0$), intermediate ($0.2 < s_0 < 0.4$), and high ($s_0 > 0.4$) degrees of order are shown alongside their corresponding F_p and HB^{inter}/HB^{tot}. (**E**) Average 1-ns MSD of all protein ($< U_{ab}^2 >$) plotted against s_0. (**F**) Average 1-ns MSD for "b"-type amorphous beads ($< U_b^2 >$) plotted against s_0. (**G**) Average 1-ns MSD for "a"-type crystalline beads ($< U_a^2 >$) plotted against s_0. MSD plotted as a function of time up to 1 ns can be reviewed for both $< U_a^2 >$ and $< U_b^2 >$ in fig. 12 for $n = 2$, $n = 8$, and $n = 16$ at each F_p.

with well-established mechanical property correlations (*23*), particularly with elastic modulus (*53*) and shear modulus (*54*). Average 1-ns MSD values of "a"-type crystal-forming beads ($< U_a^2 >$), "b"-type amorphous beads ($< U_b^2 >$), and all protein beads ($< U_{ab}^2 >$) are therefore measured and plotted as a function of s_0 in Fig. 3 (E to G). Lower $< U_b^2 >$ indicates that there is far less deviation in position for "a"-type beads than "b"-type beads since those domains are not stabilized by the hydrogen bonding potential. MSD can be decreased by increasing either MW or s_0 independently such that the smallest MSD will occur at high MW and high s_0.

Reproduction of simulated mechanical property envelope trends through postspin drawing

After applying F_p to attain a distribution of variably ordered systems, we performed uniaxial tensile deformation simulations to characterize mechanical properties correlated with s_0. Tensile tests for each MW are summarized in Fig. 4 (A to C). Stress-strain curves are plotted only up to the strain at maximum stress (ϵ_m) to draw attention to the shift in mechanical properties as s_0 increases. Of at least four independently processed tensile testing runs for simulations ranging from moderately to highly ordered, one curve with mechanical properties the closest to the average is selected and plotted in Fig. 4. The entire stress-strain curves for all simulation runs can be inspected in figs. S6 to S8. Since the solvent molecules were not removed before mechanical property measurement, we do not expect the results to be quantitative measures of an equivalent synthetic wet-spun fiber. Instead, we seek to correlate property trends captured in simulations with those obtained through experimental fiber spinning as a step toward end-to-end modeling of the protein-based fiber spinning process.

With that in mind, there is a nearly 100-fold increase in maximum stress (σ_m) between the $n = 2$ system with $s_0 = 0.92$ and the $n = 8$ system with lower order, $s_0 = 0.57$. The $n = 16$ system with the highest studied average order $s_0 = 0.47$ was 250% stronger than the $n = 8$ system with order $s_0 = 0.57$ with a nearly 4× increase in ϵ_m, which reinforces the previously established significance of MW on the strength and toughness of spider silk fibers.

For each MW, there is a clear inverse correlation between ϵ_m and σ_m where ϵ_m decreases as σ_m is enhanced through ordering and extension of individual proteins achieved during the drawing process. Since $n = 2$ systems have much lower performance, it is difficult to see how their properties correlate with s_0 compared to the $n = 8$ and $n = 16$ systems. The same order-mechanical property relationships, which are presented in Fig. 5, are plotted with a secondary y axis for the $n = 2$ case in fig. S16. The trends are consistent across MW, where σ_m and elastic modulus (E_y) are positively correlated with s_0, while ϵ_m is negatively correlated. Toughness, or deformation energy (U_T) up to maximum strain, has an initial marked increase with s_0 before leveling off in the $n = 8$ case and continuing to increase gradually for $n = 16$ systems.

Recently, incorporation of molecular-level descriptors such as MSD, also known as protein *B*-factor, has been shown to enhance mechanical property prediction capabilities of sequence-based machine learning models (*23*). The impact of change in *B*-factor on the predicted change in tensile strength and breaking strain of natural silk fibers is reported in fig. S17 using the data-constrained deep learning framework detailed by Pandey *et al.* (*23*). Our simulations show that for the more mechanically robust $n = 8$ and $n = 16$ simulations, $< U_{ab}^2 >$ has a strong correlation with changes in ϵ_m and σ_m (Fig. 5, E and F). This trend also holds somewhat for the $n = 2$

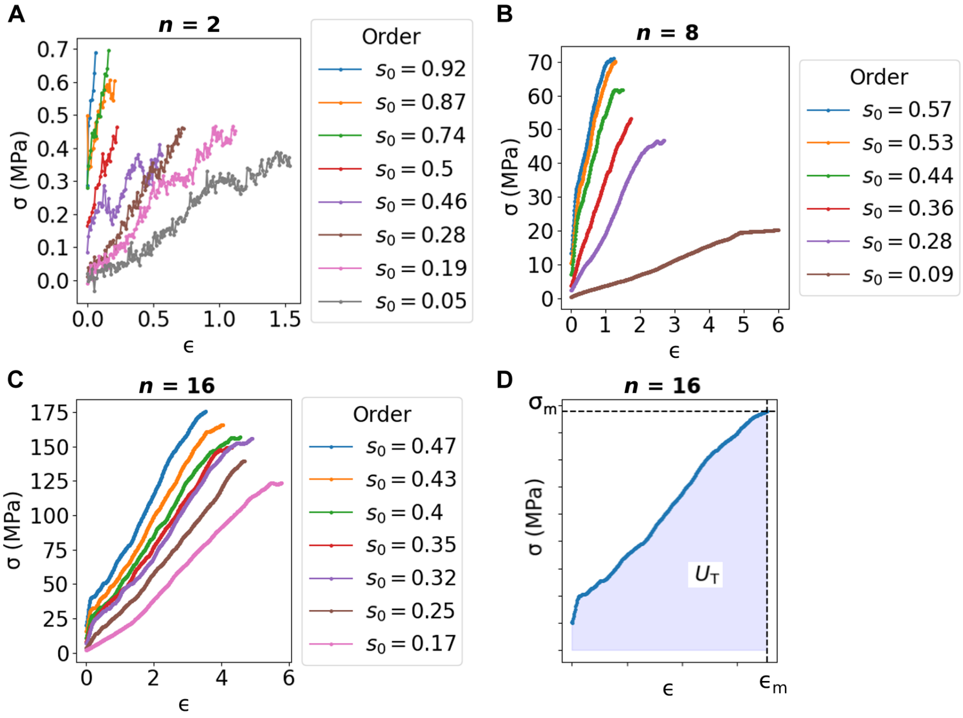

Fig. 4. Select representative tensile tests plotted up to maximum stress (σ_m). (**A**) $n = 2$–, (**B**) $n = 8$–, and (**C**) $n = 16$–repeat spider silk simulations labeled by the average s_0 achieved by each F_p. (**D**) A reference curve is provided to define maximum stress, strain at maximum stress (ϵ_m), and toughness up to maximum stress (U_T) as they will be referred to throughout this article.

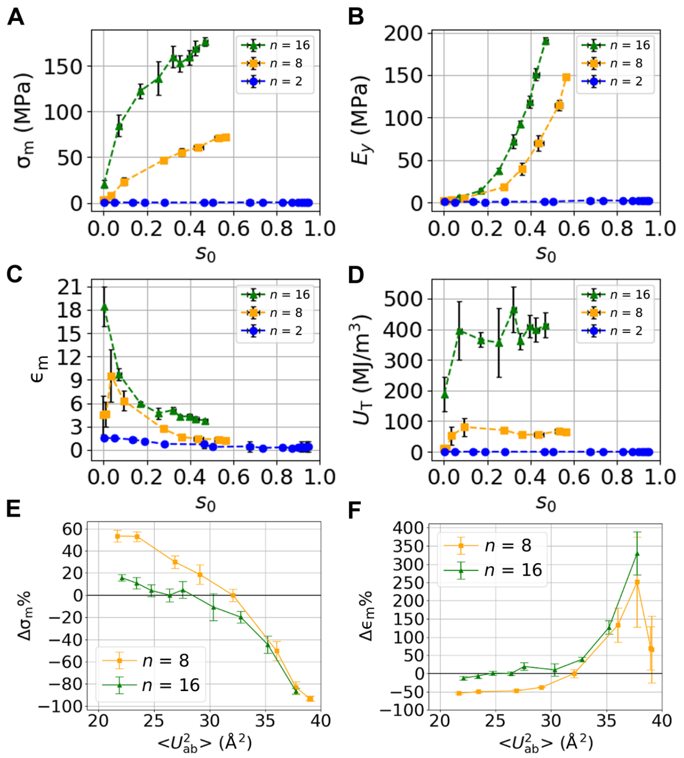

Fig. 5. Summary of mechanical property data derived from deformation simulations plotted as a function of s_0. (**A**) σ_m (MPa), (**B**) E_y (MPa), (**C**) ϵ_m, (**D**) U_T (MJ/m^3). (**E**) Percent change in σ_m ($\Delta\sigma_m$%) plotted as a function of $< U^2_{ab} >$ as compared to an intermediate reference value of $< U^2_{ab} >$ for $n = 16$ and $n = 8$. (**F**) Percent change in ϵ_m ($\Delta\epsilon_m$ %) plotted as a function of $< U^2_{ab} >$ as compared to an intermediate reference value of $< U^2_{ab} >$ for $n = 16$ and $n = 8$. The total toughness through the entire simulation is plotted in fig. S9.

systems but with far more error and less variation overall in mechanical properties (fig. S9).

Using the recombinant method for synthesizing spider silk fibers outlined in Fig. 6A, we were able to compare mechanical property trends obtained in drawn spider silk simulations with wet-spun fibers drawn to varying draw ratios (λ_{draw}). Since the silk fibers could be reliably drawn to $\lambda_{draw} = 6$ without breaking them, this was the range over which uniaxial tensile deformations were compared to the simulated λ_{ee}-property relationships for $n = 16$ proteins. Figure 6 (B to E) and figs. S11 and S12 summarize results of mechanical characterization of 16-repeat amyloid-silk proteins (16xFGA), which differ from the consensus sequence of *N. clavipes* mainly in that the polyalanine domain is replaced by a β amyloid of the sequence FGAILSS to improve protein expression (*4*, *20*, *55*, *56*). A necessary minimum draw ratio to overcome the initial brittle behavior of as-spun 16xFGA fibers ($\lambda_{draw} = 3$) in this case is consistent with previous observations of wet-spun silk fibers (*42*). After an initial toughening of the fibers beyond $\lambda_{draw} > 3$, U_T fluctuates somewhat without a clear relationship with λ_{draw}, while ϵ_m and σ_m continue to increase steadily.

To quantify the degree of β crystal alignment along the fiber axis, polarized Raman spectra were collected with fibers oriented both perpendicular (I_y) and parallel (I_x) to the direction of laser polarization (*57*). Average normalized Raman intensities, I_y and I_x, are plotted against wavenumber for each draw ratio in fig. S13. The peak intensity ratio ($I_{y/x}$), comparing intensities of the amide I β sheet peak at 1670 cm^{-1} between the parallel and perpendicular positions, is reported in Fig. 7B as a function of λ_{draw}, showing that the alignment of the crystalline region substantially improves with drawing. This alignment-extension relationship is consistent with the relationships between s_0 and λ_{ee} achieved in simulations of the $n = 16$ systems (Fig. 7A). Good agreement in mechanical property trends between simulated systems and wet-spun fibers follows in Fig. 7 (C to F) with the exception of brittle behavior at low draw ratios, which is not observed in simulations of $n = 16$ fibers. To further validate the agreement in property trends between experiments and simulations, another protein was spun into fibers and characterized similarly. We used the ^{N}M-16xFGA-^{C}M protein (*20*), which has a split mussel foot protein 5 fused to the N and C termini of the 16xFGA protein. Summaries of the mechanical characterization and comparison of experimental and simulated results are available in figs. S14 and S15. The maximum ratio to which fibers could be drawn before breaking was $\lambda_{draw} = 6$, which is consistent with the maximum postspin draw ratio observed in previous studies of synthetic spider silk (*58*, *59*). The inability to capture the brittle failure of undrawn fibers is ascribed to ductility induced by the high water content of simulated fibers, which are still semisolubilized. Establishing a computational protocol for replicating the solvent exchange and drying processes of synthetic silk production is left to subsequent papers.

Although the dependence of mechanical properties on order and extension is evident from the results presented in this work, a theory that links specific features that are only quantifiable through either simulations or experiments is required to accurately predict the properties of silk fibers on the basis of sequence and processing. The group interaction modeling framework can be used to phenomenologically describe the spider silk mechanical property envelope for various dragline silks as a function of a single model variable, the ordered fraction f_{ord} (*32*). In that study, the authors postulated that for a particular repetitive sequence of spider silk, the negative correlation between σ_m and ϵ_m was attributed to changes in f_{ord} of silk. The mechanisms behind shifting f_{ord} and what that variable truly represents however were ambiguous, challenging the reader to imagine a more complex description of the distinctions between ordered and disordered protein regions. The results here draw attention to some measurable features: s_0, R_{ee}, $< U^2 >$, and HB^{inter}/HB^{tot}, which are strongly correlated with f_{ord}, suggesting that a multifarious description of order could be reduced to a function of a few such features. In a step toward achieving this goal, we established a theoretical description of the 16xFGA fibers inspired by group interaction modeling. Our progress is outlined in Supplementary Text.

DISCUSSION

As the accessibility of data-hungry machine learning methods grows, so does the demand for large libraries linking target properties to critical design features across scientific fields. In the case of spider silk, there are limited data connecting mechanical property data to the primary amino acid sequence (*14*), and there are even less data that consider processing and sequence parameters simultaneously. Models to predict physical properties of materials can be enriched through incorporation of simulation-derived relationships between *B*-factor, order, chain conformation, and mechanical properties. Here, we proposed a method for detecting the dependence of synthetic silk fiber mechanical properties on order and extension arising from postspin

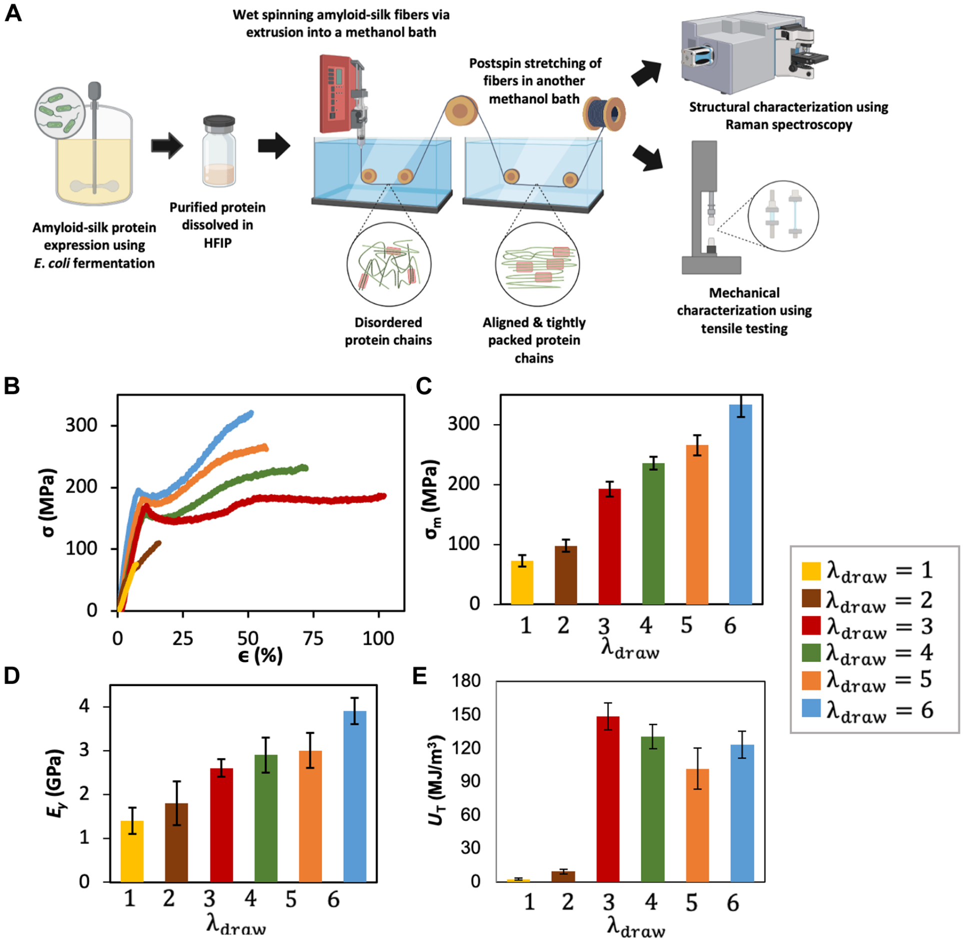

Fig. 6. Recombinant amyloid-silk protein synthesis, fiber wet spinning, and characterization. (**A**) Schematic representation of recombinant 16xFGA protein fiber production. The 16xFGA proteins were biosynthesized by engineered bacteria and purified before being dissolved into HFIP. The dopes were extruded into a coagulation bath containing 95% methanol to form monofilament fibers. The spun fibers were subjected to an additional stretching step in a 75% methanol bath to promote protein alignment. To study the effect of different stretch ratios on fiber properties, individual fiber pieces (~5 cm in length) were manually stretched to several times their original length (two to six times). The stretched fibers were then mechanically and structurally characterized using tensile testing and Raman spectroscopy, respectively. (**B**) Representative stress-strain curves from tensile testing of the 16xFGA protein fibers at different stretch ratios. (**C** to **E**) Comparison of (C) σ_m, (D) E_y, and (E) U_T of 16xFGA protein fibers at different stretch ratios (λ_{draw}).

drawing using a computationally inexpensive coarse-grained molecular dynamics approach. Previous efforts at modeling spider silk with all-atomistic representations have provided fundamental insights on the mechanical behavior of silk nanostructure (*60*–*62*), strain-induced β sheet structural transitions (*63*), self-assembly in hydrodynamic flow (*30*), and even bulk mechanical properties of spider silk (*64*). Our proposed processing method captures critical elements of these models including extension-induced enhancement of overall crystallinity, interprotein hydrogen bonding, and ordering of proteins along the fiber axis. At the same time, the simulated drawing process recreates the order-dependent mechanical property envelope that gives silk-based materials their processing-dependent tunability. The inspiration for this work came after we recreated the data from a paper using this silk DPD model to demonstrate that shear flow substantially increased the order of domains tethering crystal aggregates (*31*). We found that those tethering domains only accounted for a small proportion of all the proteins in the system. Most proteins remained in a globular state with short R_{ee} and low s_0, squandering unrealized potential for extension and ordering. To contextualize our work with theirs, a description of how different combinations of F_p and shear flow rate ($\dot{\gamma}$) during processing affect order, end-to-end length, and hydrogen bonding is summarized in fig. S17 (B to E). Figure S17A shows how a single system can access the full extent of the mechanical property envelope through variation of two processing parameters. However, phenomena such as an increase in elastic modulus of shear-processed fibers over fibers that are processed purely with the drawing pull force warrant more detailed analysis of yield mechanisms in tensile tests and validation with experiments that covary shear rate and draw ratio. These results emphasize the synergy between shear flow and application of drawing forces during the fiber-forming process. The seminal work introducing this DPD model of silk, carried out by Lin *et al.* (*27*), inspired Shen *et al.* to develop a full-atomistic model of a spider silk fiber (*64*). Shen *et al.* used the predicted distribution of shear flow–assembled crystals and the network connecting them to manually build an all-atomistic continuum of silk crystals embedded in an amorphous matrix. They used their full-atomistic model to investigate the impact of prestretching on mechanical properties, but their efforts were limited by a lack of solvent. Breaking strain decreased with increasing breaking strength as a function of prestretched ratio under the dry prestretching condition, but fiber toughness decreased, which contrasts with the simulated and synthesized fibers for this manuscript. This indicates that solvent is a necessary element of silk drawing molecular models for its role in enhancing interprotein hydrogen bonding and facilitating β sheet reorganization. Another notable difference between these two studies was the nonequilibrium molecular dynamics strategy used to simulate drawing. In the full-atomistic model, the entire simulation box was deformed uniformly to prestretch the fiber, whereas here, we apply a homogeneous force to each protein in the system to precisely control their degree of extension. From a modeling perspective, the uniform box deformation strategy markedly narrows the simulation box dimensions, which can cause boundary effects to play a role at lower strains in uniaxial tensile tests. However, it more directly mimics the drawing process than the artificially induced pull force. Both strategies should be considered and compared more directly in future studies while including solvent during prestretching.

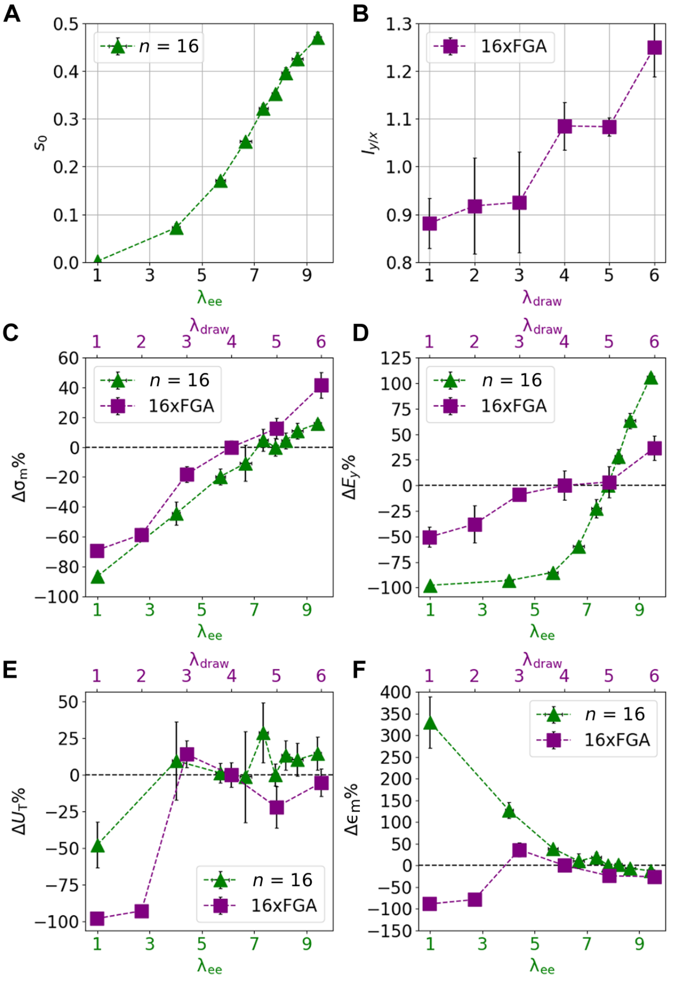

Fig. 7. Comparison of the relationships between molecular order, degree of stretch, and mechanical properties in simulations and experiments. (**A**) s_0 plotted as a function of λ_{ee} as measured in simulations of $n = 16$ systems. (**B**) Peak intensity ratio of the amide I peak from Raman spectroscopy quantified for 16xFGA fibers as a function of λ_{draw}. (**C** to **F**) Comparison of percent change in mechanical properties as they vary with stretch parameters in simulations and experiments with λ_{ee} plotted on the primary *x* axis and λ_{draw} plotted on the secondary *x* axis for (C) $\Delta\sigma_m\%$, (D) $\Delta E_y\%$, (E) $\Delta U_T\%$, and (F) $\Delta\epsilon_m$ %.

Although this method currently lacks primary sequence-level resolution, there is potential for the implementation of systematic coarse-graining approaches such as the energy renormalization method (*54*, *65*, *66*), which could be used to introduce primary-sequence features to this already process-sensitive workflow. The repulsive DPD parameters of hydrophobic and hydrophilic bead types in this model are largely qualitative, having been borrowed from a generalized DPD model of copolymers in solvent (*37*, *38*). This has proven sufficient in linking process-dependent polymer conformation and assembly to mechanical properties. However, a more thorough and conventional approach of deriving coarse-grain force field parameters from linking force field parameters to all-atomistic simulation is necessary to extract sequence-property relationships from simulation. While the coarse-graining process would itself be computationally intensive, the expansion of parameters would not substantially decrease the efficiency of this simulated silk processing workflow.

A notable limitation of this model is its omission of the final extrusion step of synthetic silk spinning, which involves solvent exchange in the case of wet spinning (*16*, *67*) or a highly viscous dope in the case of dry spinning (*68*, *69*). The biggest consequence of leaving out this processing step is the time dependence of *s* and R_{ee} through the relaxation step after s_0 has been measured. Because the solvent particles remain during the tensile deformation, the stress-strain profiles likely underpredict the true strength and stiffness of silk fibers by maintaining the relative conformational freedom that polymers have in solvent. The presence of solvent during tensile tests may also explain the large deformations up to many times the initial fiber length, which are inconsistent with synthetic fibers that stretch to a maximum of double their initial length. Along with implementation of a systematic coarse-grain framework, this model would benefit from a solvent exchange model by which hydrophilic solvent particles are replaced by hydrophobic particles. This process would induce the rapid protein assembly that occurs during extrusion into nonpolar solvent like hexafluoroisopropanol (HFIP). The drying process could then be modeled by gradually removing solvent particles and relaxing the system between particle deletions. These additions would be an important step toward modeling the aqueous environment and solvents experienced by silk proteins in both the natural and synthetic silk-spinning processes (*70*). The brittle behavior of undrawn wet-spun fibers is a common challenge, which severely decreases the maximum strength and toughness of synthetic fibers. This behavior is unique to synthetic silk. Natural silk undergoes a drawing force whether it is forcibly reeled or pulled out of the silk gland by the spider's own hind legs. Without a drawing step, proteins are immobilized by increased entanglements, which are made permanent upon drying. Undrawn fibers therefore break abruptly when a load is applied since the chains cannot elongate and reorient during the deformation. In simulations, mobility is always conferred by the presence of solvent. Observing the mechanisms of brittle failure in undrawn silk fibers would therefore require a model that accounts for the drying process of the undrawn fibers compared to drawn fibers. This phenomenon will be studied further when a suitable strategy for removing solvent particles is devised. The continuous model of an anisotropic network of silk peptides in solvent also fails to consider fracture mechanisms that are related to impurities and cracks that form at the interface of the silk fiber shell and air. Consistent manufacturing of silk fibers requires that the spun silk is exposed to a consistent ambient environment with minimal particulates, which can disrupt the integrity of the fiber shell during drying. Variation in mechanical properties derived from simulations was also observed, which, in some cases, introduced substantial uncertainty in the measurements. Those variations are summarized by the error bars representing standard deviation across five runs in Fig. 5. Within simulations that were processed with the same conditions, but with different starting configurations, we could not find any variables that consistently correlated with fluctuations in mechanical properties. Variability within processing conditions must be either a function of many of the parameters quantified in this study or because of some spatial variability that causes weak points in the simulation box. Such spatial variability could be mitigated by either expanding the size of the simulation or improving the homogeneity of the simulation by removing solvent. Nonetheless, our work serves as an augmentation to existing silk modeling strategies and will hopefully inspire further improvements toward developing sequence-process-property prediction methods for silk and other biological materials.

MATERIALS AND METHODS

Modeling drawn silk

The workflow for modeling silk peptides using a DPD representation was adapted directly from previous publications that outlined step-by-step instructions for synergistic coupling of modeling and biomimetic silk spinning for protein design. While all files necessary for setup, equilibration, and tensile tests are available for download from Rim *et al.* (*28*), the pull force processing steps were added and included in a GitHub codebase made available alongside this publication. This codebase includes instructions and all functionality of the original work, with certain augmentations that are detailed in the README file seeking to modernize software used, add analysis, and improve overall accessibility. Appropriate citation requests are listed at the beginning of the README file to attribute the original works (*27*, *28*), but we believe that the format of a hosted repository makes it easier for researchers to revise this tool to suit their needs and recommend it for researchers seeking to reproduce and refine this work.

DPD simulations were performed using LAMMPS (Large-scale Atomic/Molecular Massively Parallel Simulator) (*71*). To generate the initial configuration of polymers in solvent, a rectangular box was populated with linear chains of coarse-grained beads of specified block size and length to achieve a protein:solvent volume fraction of 20:80 and a number density of three. Protein chains were grown randomly while fixing the initial distance between beads to the equilibrium bond distance. The box size for $n = 2$ simulations was 60 by 40 by 40 R_c^3, where $R_c = 9.321$ Å, the characteristic length previously derived for this DPD model. For $n = 8$ and $n = 16$ simulations, the box size was increased incrementally to 100 by 80 by 80 R_c^3 and 160 by 80 by 40 R_c^3 to avoid chains crossing periodic boundaries with the long dimension oriented parallel to the direction of pull force–induced protein extension.

Simulations to mimic the properties of drawn silk were carried out in an NVE ensemble using a time step of $\Delta t = 0.03\tau$, with $\tau = 0.75$ ns being the previously established characteristic timescale of the DPD model (*27*). The equilibration run of 420,000 time steps was twice as long as the value of 210,000 time steps prescribed by Rim *et al.* to achieve a steady state by root-mean-square-deviation tracking for systems of similar size and composition. A range of pull forces F_p was then applied to achieve a range of s_0 values ahead of uniaxial tensile tests. At the end of the equilibration step, both ends of each protein were identified as being the closest to the left-most or right-most end of the box along its long axis. Equal and opposite pull forces were then applied such that the two ends were pulled away from each other. An appropriate range of force values was selected on the basis of force-extension curves derived from single-molecule AFM experiments conducted on spider silk fibers (*45*). Since this model has no appropriate criterion for bond breaking, we wanted to study only those pull forces required to unravel the protein. In the postspin drawing process, there are certain structures held so strongly together by entanglements and β crystals that an individual protein could not be pulled out of that structure without breaking first. Without a bond breaking criterion, we decided to study the whole range of pull forces up to the point at which an individual synthetic silk protein unravels. Single-molecule force microscopy experiments previously performed on a 16-repeat synthetic sequence containing MaSp1 and major ampullate spidroin 2 (MaSp2) of *N. clavipes* showed that the unraveling force of individual proteins could reach ~220 pN. AFM peaks greater than 220 pN were attributed to multiple protein molecules being attached to the tip of the AFM probe (*45*), so the maximum pull force used in simulating drawing was $F_p = 50$ LJ = 222 pN. For the DPD model, dimensionless units of force are given by $R_c / (k_B T) = 1$ such that one unit of Lennard-Jones dimensionless force (LJ) is equal to 4.44 pN real units at 300 K. The pull forces studied therefore fell within 0 pN < F_p < 222 pN. For $n = 2$ systems, the pull force processing step lasted for 1,680,000 steps for 0 pN < F_p <= 19.98 pN. This value was reduced to 840,000 steps for F_p > 19.98 pN since s and R_{ee} were unchanging after so many steps (see fig. S1). The pull force processing step was increased to 2,100,000 and 3,360,000 steps, respectively, for the $n = 8$ and $n = 16$ systems because of slower response times of s and R_{ee} to pull force (see Fig. 2, A and B, and fig. S2).

After each system was processed via pulling force, a relaxation was carried out for 150,000 Δt to observe the impermanence of s and R_{ee} in solvent before uniaxial tensile tests were performed. Effective stress normal to the pull force and ultimately uniaxial deformation was computed by the strategy reported in the "Modeling silk mechanical properties" section. Effective stress was measured during the relaxation to quantify the degree of stress imposed by F_p and to identify the residual stress leading into uniaxial tensile tests. Stress throughout the relaxation step is reported for $n = 2$, $n = 8$, and $n = 16$ systems, respectively, in figs. S18 to S20.

Molecular dynamics trajectory analyses

The open-source Python library MDAnalysis (*72*, *73*) was used to calculate hydrogen bond counts, MSD (*74*, *75*), R_{ee}, and s. Two "a"-type beads were defined as forming a hydrogen bond with one another when the distance between them fell within the nonbonded harmonic potential cutoff distance, $R_c = 1$ LJ = 0.9321 nm. Contacts identified on the basis of this criterion that were directly connected by a covalent bond were excluded from analysis. MSD values were computed using the Einstein formula, as it is outlined in the documentation for the MDAnalysis.analysis.msd module (*75*). R_{ee} was measured as the distance between the first bead and the last bead in each protein. Each R_{ee} measurement was the average of a random sample of 100 chains tracked throughout the trajectory. s was computed for the same sample of 100 chains throughout the trajectory and computed from Eq. 1

$$s = \frac{1}{2} < 3\cos^2\Theta - 1 > \tag{1}$$

Here, Θ refers to the angle between the fiber axis and the vector representing the covalent bond between adjacent beads in a protein. The brackets indicate an average over all the bonds in a single protein.

Modeling silk mechanical properties

Uniaxial tensile tests were run by deforming the simulation box with proteins and solvent along the same axis as ordering and extension using the LAMMPS fix deform command. In accordance with the fixed volume thermodynamic ensemble, the dimensions perpendicular to the pulling direction were adjusted simultaneously while maintaining a fixed aspect ratio. Simulations were deformed to a maximum strain of $\epsilon = 9$ over 1,000,000 time steps, which converts to a constant engineering strain rate of $3 \times 10^{-4}\ \tau^{-1}$. In some low–pull force cases, this tensile test was extended up to $\epsilon = 27$ to identify large failure strains and U_T up to those values. Refer to figs. S7 and S8 to see all simulated tensile test results. Effective stress was calculated using the strategy outlined in previous work, by which the effective stress is computed as a function of the normal stress tensor σ_i ($i = x, y, z$) using Eq. 2, which is the stress (σ) that we report throughout this paper. Equation 2 assumes a Poisson's ratio of $\nu = 0.5$ for a material undergoing constant volume uniaxial deformation along the x axis

$$\sigma = \sigma_{\text{eff}} = \sigma_x - \nu\left(\sigma_y + \sigma_z\right) \tag{2}$$

The elastic modulus E_y can then be computed using Eq. 3, where E_y is the notation for Young's or elastic modulus throughout this paper (*27*)

$$\text{Young's modulus } \left(E_y\right) = E_x = \frac{\sigma_x - \nu\left(\sigma_y + \sigma_z\right)}{\epsilon_x} \tag{3}$$

The Δσ between the regions of ~5 to 9% was used to calculate E_y in simulations. The strategy to remove the effect of solvents described by Lin *et al.* involves dividing E_x with the ratio between the volume of the whole simulation box and the effective volume occupied by polymers (*27*). To convert DPD units of stress/pressure to real units, dimensionless stress, $k_B T / R_c^3 = 1$, was translated to physical units of 5.11 MPa at the temperature of 300 K used in simulations.

For the $n = 8$ and $n = 16$ systems, maximum strain and maximum stress were collected from at least four tensile tests starting from independently processed configurations, which are summarized in figs. S14 and S15. The toughness U_T is computed by numerical integration of the area under the stress-strain curve using the trapezoid rule up to ϵ_m, as defined in Fig. 4D.

For $n = 2$ systems, tensile tests were again collected from at least four tensile tests starting from independently processed configurations, but failure occurred before $\epsilon = 2$ in every case (fig. S6. Mechanical properties ϵ_m and σ_m were therefore defined as the maximum achieved before $\epsilon < 2$. U_T was calculated using the same method as was used for $n = 8$ and $n = 16$ systems.

Recombinant silk fiber synthesis

Escherichia coli strain NEB 10-beta (NEB10β) transformed with the suitable plasmid was used for protein production. Protein 16xFGA was expressed from plasmid pJL464 reported in previous studies (*4*, *20*, *55*). During protein expression, *E. coli* strains were grown in Terrific Broth (TB) containing yeast extract (24 g liter^{-1}), tryptone (20 g liter^{-1}), 0.4% (v/v) glycerol, 17 mM KH_2PO_4, and 72 mM K_2HPO_4, with incubation at 37°C and constant shaking. Appropriate antibiotics [ampicillin (50 μg ml^{-1})] were added as needed. A single colony of a suitable strain was inoculated into TB medium and cultivated at 37°C on an orbital shaker. Subsequently, this culture was used to inoculate a fresh TB medium, which was allowed to grow until it reached an optical density of 0.6 as measured by the absorbance at 600 nm (OD_{600}). To induce protein expression, 0.04% arabinose was added, and the culture was continued at 37°C for 24 hours. Afterward, cells were harvested by centrifugation at 3500 rpm, and the resulting cell pellets were preserved at −80°C for later use. Cell pellets were subjected to lysis in buffer A (6 M guanidine hydrochloride, 300 mM NaCl, and 50 mM K_2HPO_4 at pH 8.0) for a duration of 12 hours at 4°C with continuous stirring. The lysate was then centrifuged, and the resulting supernatant was loaded onto a Ni-NTA column. This column was subsequently washed sequentially with buffer B (8 M urea, 300 mM NaCl, and 50 mM K_2HPO_4 at pH 8.0) using imidazole concentrations of 0, 20, and 50 mM. The proteins were eluted using buffer B containing 300 mM imidazole. All the purified proteins were dialyzed in 1% acetic acid, lyophilized, and stored at −80°C for later use. Lyophilized protein powders were dissolved in HFIP to create spinning dopes at a concentration of 15% (w/w). These dopes were loaded into a 100-μl syringe from Hamilton Robotics and extruded slowly into a bath of 95% (v/v) methanol. The extrusion was controlled by a Harvard Apparatus Pump 11 Elite Syringe Pump from Harvard Apparatus, which delivered the dopes at a rate of 10 μl min^{-1}. The extruded fibers were then placed in a 75% (v/v) methanol bath and gently elongated to different lengths, as indicated in the manuscript. After extension, the fibers were removed from the methanol bath and allowed to air dry.

Recombinant silk fiber mechanical testing

Fiber diameters were assessed using a Zeiss Axio Observer ZI inverted microscope, which was equipped with a 20× phase-contrast objective lens. The measurements were quantified using Axiovision LE software from Zeiss. Sections of postdrawn fibers, each measuring 20 mm in length, were deliberately placed in a precisely vertical orientation across a rectangular opening cut into a 20 mm–by–20 mm piece of cardstock. This opening had dimensions of 5 mm in height (vertical) and 15 mm in width (horizontal). The fibers were secured in place using adhesive tape at both ends of the opening. Tensile tests were carried out using an MTS Criterion Model 41 Universal Test Frame equipped with a 1-N load cell from MTS Systems Corporation. The tests were conducted at a room temperature of 25°C and a relative humidity of 20%, with a constant pulling speed of 10 mm min^{-1}. The ultimate tensile strength was calculated as the maximum load applied to the initial cross-sectional area of the fiber, assuming that the cross section was circular. The modulus was determined as the slope of the initial elastic region on the stress-strain curve using linear least-squares fitting. The ultimate breaking strain was calculated as the percentage of fiber elongation relative to the initial gauge length (5 mm) before the fiber broke. The toughness was computed as the area under the entire stress-strain curve. Stress-strain curves were recorded by the MTS TW Elite Test Suite at a sampling rate of 50 Hz.

Recombinant silk fiber alignment characterization

The method used for polarized Raman spectromicroscopy was adapted from a previous study on molecular alignment in spider silk fibers (*57*). Single composite fiber pieces were securely affixed to glass microscope slides marked with microscale indicators to ensure that spectra were acquired from the same location before and after stage rotation. Raman spectra were collected using a Renishaw RM1000 InVia Confocal Raman Spectrometer connected to a Leica DM LM microscope featuring a rotating stage. Initially, fibers were oriented along the x axis, parallel to the laser polarization. A fixed point on the fibers was irradiated using the 514-nm argon laser line with the laser polarization oriented along the x axis. This was done through a 50× objective (numerical aperture, 0.75), and spectra were recorded in the range of 1100 to 1800 cm^{-1} with 1800 lines per millimeter grating. Each acquisition involved accumulating a total of 10 spectra, each recorded for 10 s. Subsequently, the stage was rotated to align the fibers along the y axis, while the laser polarization remained the same, and spectra were recorded again at the same fixed point. No signs of thermal degradation were observed, either visually or within the recorded spectra. Fityk 0.9.865 was used for baseline corrections using its automatic convex hull algorithm (*76*). For intensity ratio calculations, all spectra were normalized to the intensity of the peak at 1450 cm^{-1}, stemming from CH_2 bending and insensitive to the protein conformation. For each fiber, the normalized intensity of the peak at 1670 cm^{-1} when oriented along the y axis was divided by the normalized intensity of the same peak when oriented along the x axis, resulting in the intensity ratio $I_{y/x}$. This procedure was conducted on three separate fibers for each condition, and the calculated intensity ratios were averaged.

Supplementary Materials

This PDF file includes:

Supplementary Materials and Methods
Supplementary Text
Table S1
Figs. S1 to S22
References

REFERENCES AND NOTES

1. J. M. Gosline, P. A. Guerette, C. S. Ortlepp, K. N. Savage, The mechanical design of spider silks: From fibroin sequence to mechanical function. *J. Exp. Biol.* **202** (Pt. 23), 3295–3303 (1999).
2. I. Agnarsson, M. Kuntner, T. A. Blackledge, Bioprospecting finds the toughest biological material: Extraordinary silk from a giant riverine orb spider. *PLOS ONE* **5**, e11234 (2010).
3. A. Koeppel, C. Holland, Progress and trends in artificial silk spinning: A systematic review. *ACS Biomater. Sci. Eng.* **3**, 226–237 (2017).
4. J. Li, Y. Zhu, H. Yu, B. Dai, Y. S. Jun, F. Zhang, Microbially synthesized polymeric amyloid fiber promotes β-nanocrystal formation and displays gigapascal tensile strength. *ACS Nano* **15**, 11843–11853 (2021).
5. M. Ramezaniaghdam, N. D. Nahdi, R. Reski, Recombinant spider silk: Promises and bottlenecks. *Front. Bioeng. Biotechnol.* **10**, 835637 (2022).
6. A. E. Thurber, F. G. Omenetto, D. L. Kaplan, In vivo bioresponses to silk proteins. *Biomaterials* **71**, 145–157 (2015).
7. S. Kumari, G. Lang, E. DeSimone, C. Spengler, V. T. Trossmann, S. Lücker, M. Hudel, K. Jacobs, N. Krämer, T. Scheibel, Engineered spider silk-based 2D and 3D materials prevent microbial infestation. *Mater. Today* **41**, 21–33 (2020).
8. K. Hennecke, J. Redeker, J. W. Kuhbier, S. Strauss, C. Allmeling, C. Kasper, K. Reimers, P. M. Vogt, Bundles of spider silk, braided into sutures, resist basic cyclic tests: Potential use for flexor tendon repair. *PLOS ONE* **8**, e61100 (2013).
9. J. Jeon, K. Z. Lee, X. Zhang, J. Jaeger, E. Kim, J. Li, L. Belaygorod, B. Arif, G. M. Genin, M. B. Foston, M. A. Zayed, F. Zhang, Genetically engineered protein-based bioadhesives with programmable material properties. *ACS Appl. Mater. Interfaces* **15**, 56786–56795 (2023).
10. K. Dastagir, N. Dastagir, A. Limbourg, K. Reimers, S. Strauß, P. M. Vogt, In vitro construction of artificial blood vessels using spider silk as a supporting matrix. *J. Mech. Behav. Biomed. Mater.* **101**, 103436 (2020).
11. M. Xu, Y. Jiang, S. Pradhan, V. K. Yadavalli, Use of silk proteins to form organic, flexible, degradable biosensors for metabolite monitoring. *Front. Mater.* **6**, 1–9 (2019).
12. J. Sun, J. Chen, K. Liu, H. Zeng, Mechanically strong proteinaceous fibers: Engineered fabrication by microfluidics. *Engineering* **7**, 615–623 (2021).
13. R. Kennedy, "Gossamer silk, from spiders spun," *The New York Times*, 22 September 2009.
14. K. Arakawa, N. Kono, A. D. Malay, A. Tateishi, N. Ifuku, H. Masunaga, R. Sato, K. Tsuchiya, R. Ohtoshi, D. Pedrazzoli, A. Shinohara, Y. Ito, H. Nakamura, A. Tanikawa, Y. Suzuki, T. Ichikawa, S. Fujita, M. Fujiwara, M. Tomita, S. J. Blamires, J. A. Chuah, H. Craig, C. P. Foong, G. Greco, J. Guan, C. Holland, D. L. Kaplan, K. Sudesh, B. B. Mandal, Y. Norma-Rashid, N. A. Oktaviani, R. C. Preda, N. M. Pugno, R. Rajkhowa, X. Wang, K. Yazawa, Z. Zheng, K. Numata, 1000 spider silkomes: Linking sequences to silk physical properties. *Sci. Adv.* **8**, eabo6043 (2022).
15. H. Poddar, R. Breitling, E. Takano, Towards engineering and production of artificial spider silk using tools of synthetic biology. *Eng. Biol.* **4**, 1–6 (2020).
16. B. Schmuck, G. Greco, T. B. Pessatti, S. Sonavane, V. Langwallner, T. Arndt, A. Rising, Strategies for making high-performance artificial spider silk fibers. *Adv. Funct. Mater.* **34**, 2305040 (2024).
17. M. B. Hinman, R. V. Lewis, Isolation of a clone encoding a second dragline silk fibroin. Nephila clavipes dragline silk is a two-protein fiber. *J. Biol. Chem.* **267**, 19320–19324 (1992).
18. C. H. Bowen, C. J. Sargent, A. Wang, Y. Zhu, X. Chang, J. Li, X. Mu, J. M. Galazka, Y. S. Jun, S. Keten, F. Zhang, Microbial production of megadalton titin yields fibers with advantageous mechanical properties. *Nat. Commun.* **12**, 5182 (2021).
19. C. H. Bowen, B. Dai, C. J. Sargent, W. Bai, P. Ladiwala, H. Feng, W. Huang, D. L. Kaplan, J. M. Galazka, F. Zhang, Recombinant spidroins fully replicate primary mechanical properties of natural spider silk. *Biomacromolecules* **19**, 3853–3860 (2018).
20. J. Li, B. Jiang, X. Chang, H. Yu, Y. Han, F. Zhang, Bi-terminal fusion of intrinsically-disordered mussel foot protein fragments boosts mechanical strength for protein fibers. *Nat. Commun.* **14**, 2127 (2023).
21. T. Arndt, G. Greco, B. Schmuck, J. Bunz, O. Shilkova, J. Francis, N. M. Pugno, K. Jaudzems, A. Barth, J. Johansson, A. Rising, Engineered spider silk proteins for biomimetic spinning of fibers with toughness equal to dragline silks. *Adv. Funct. Mater.* **32**, 2200986 (2022).
22. J. Johansson, A. Rising, Doing what spiders cannot—A road map to supreme artificial silk fibers. *ACS Nano* **15**, 1952–1959 (2021).
23. A. Pandey, W. Chen, S. Keten, Sequence-based data-constrained deep learning framework to predict spider dragline mechanical properties. *Commun. Mater.* **5**, 83 (2024).
24. W. Finnigan, A. D. Roberts, C. Ligorio, N. S. Scrutton, R. Breitling, J. J. Blaker, E. Takano, The effect of terminal globular domains on the response of recombinant mini-spidroins to fiber spinning triggers. *Sci. Rep.* **10**, 10671 (2020).
25. D. N. Breslauer, L. P. Lee, S. J. Muller, Simulation of flow in the silk gland. *Biomacromolecules* **10**, 49–57 (2009).
26. F. Paquet-Mercier, T. Lefèvre, M. Auger, M. Pézolet, Evidence by infrared spectroscopy of the presence of two types of β-sheets in major ampullate spider silk and silkworm silk. *Soft Matter* **9**, 208–215 (2013).
27. S. Lin, S. Ryu, O. Tokareva, G. Gronau, M. M. Jacobsen, W. Huang, D. J. Rizzo, D. Li, C. Staii, N. M. Pugno, J. Y. Wong, D. L. Kaplan, M. J. Buehler, Predictive modelling-based design and experiments for synthesis and spinning of bioinspired silk fibres. *Nat. Commun.* **6**, 6892 (2015).
28. N. G. Rim, E. G. Roberts, D. Ebrahimi, N. Dinjaski, M. M. Jacobsen, Z. Martín-Moldes, M. J. Buehler, D. L. Kaplan, J. Y. Wong, Predicting silk fiber mechanical properties through multiscale simulation and protein design. *ACS Biomater. Sci. Eng.* **3**, 1542–1556 (2017).
29. O. S. Tokareva, S. Lin, M. M. Jacobsen, W. Huang, D. Rizzo, D. Li, M. Simon, C. Staii, P. Cebe, J. Y. Wong, M. J. Buehler, D. L. Kaplan, Effect of sequence features on assembly of spider silk block copolymers. *J. Struct. Biol.* **186**, 412–419 (2014).
30. A. M. Herrera-Rodríguez, A. K. Dasanna, C. Daday, E. R. Cruz-Chú, C. Aponte-Santamaría, U. S. Schwarz, F. Gräter, The role of flow in the self-assembly of dragline spider silk proteins. *Biophys. J.* **122**, 4241–4253 (2023).
31. M. M. Jacobsen, O. S. Tokareva, D. Ebrahimi, W. Huang, S. Ling, N. Dinjaski, D. Li, M. Simon, C. Staii, M. J. Buehler, D. L. Kaplan, J. Y. Wong, Effect of terminal modification on the molecular assembly and mechanical properties of protein-based block copolymers. *Macromol. Biosci.* **17**, 1700095 (2017).
32. D. Porter, F. Vollrath, Z. Shao, Predicting the mechanical properties of spider silk as a model nanostructured polymer. *Eur. Phys. J. E Soft Matter* **16** (2), 199–206 (2005).
33. F. Vollrath, D. Porter, Spider silk as a model biomaterial. *Appl. Phys. Mater. Sci. Process.* **82**, 205–212 (2006).

34. A. Pandey, E. Liu, J. Graham, W. Chen, S. Keten, B-factor prediction in proteins using a sequence-based deep learning model. *Patterns* **4**, 100805 (2023).
35. M. Xu, R. V. Lewis, Structure of a protein superfiber: Spider dragline silk. *Proc. Natl. Acad. Sci. U.S.A.* **87**, 7120–7124 (1990).
36. R. V. Lewis, Spider silk: Ancient ideas for new biomaterials. *Chem. Rev.* **106**, 3762–3774 (2006).
37. Y.-J. Sheng, T.-Y. Wang, W. M. Chen, H.-K. Tsao, A–B diblock copolymer micelles: Effects of soluble-block length and component compatibility. *J. Phys. Chem. B* **111**, 10938–10945 (2007).
38. J. R. Spaeth, I. G. Kevrekidis, A. Z. Panagiotopoulos, A comparison of implicit- and explicit-solvent simulations of self-assembly in block copolymer and solute systems. *J. Chem. Phys.* **134**, 164902 (2011).
39. T. Scheibel, Spider silks: Recombinant synthesis, assembly, spinning, and engineering of synthetic proteins. *Microb. Cell Fact.* **3**, 14 (2004).
40. F. Vollrath, D. P. Knight, Liquid crystalline spinning of spider silk. *Nature* **410**, 541–548 (2001).
41. J. Pérez-Rigueiro, M. Elices, G. Plaza, J. I. Real, G. V. Guinea, The effect of spinning forces on spider silk properties. *J. Exp. Biol.* **208**, 2633–2639 (2005).
42. M. Sun, Y. Zhang, Y. Zhao, H. Shao, X. Hu, The structure-property relationships of artificial silk fabricated by dry-spinning process. *J. Mater. Chem.* **22**, 18372–18379 (2012).
43. M. Frydrych, A. Greenhalgh, F. Vollrath, Artificial spinning of natural silk threads. *Sci. Rep.* **9**, 15428 (2019).
44. J. Guan, Y. Wang, B. Mortimer, C. Holland, Z. Shao, D. Porter, F. Vollrath, Glass transitions in native silk fibres studied by dynamic mechanical thermal analysis. *Soft Matter* **12**, 5926–5936 (2016).
45. E. Oroudjev, J. Soares, S. Arcidiacono, J. B. Thompson, S. A. Fossey, H. G. Hansma, Segmented nanofibers of spider dragline silk: Atomic force microscopy and single-molecule force spectroscopy. *Proc. Natl. Acad. Sci. U.S.A.* **99**, 6460–6465 (2002).
46. A. Larrañaga, E. Lizundia, "Chapter 15 - Strain-induced crystallization," in *Crystallization in Multiphase Polymer Systems*, S. Thomas, M. Arif P., E. B. Gowd, N. Kalarikkal, Eds. (Elsevier, 2018), pp. 471–508; www.sciencedirect.com/science/article/pii/B9780128094532000153.
47. C. Riekel, B. Madsen, D. Knight, F. Vollrath, X-ray diffraction on spider silk during controlled extrusion under a synchrotron radiation X-ray beam. *Biomacromolecules* **1**, 622–626 (2000).
48. Y. Yao, B. J. Allardyce, R. Rajkhowa, C. Guo, X. Mu, D. Hegh, J. Zhang, P. Lynch, X. Wang, D. L. Kaplan, J. M. Razal, Spinning regenerated silk fibers with improved toughness by plasticizing with low molecular weight silk. *Biomacromolecules* **22**, 788–799 (2021).
49. B. An, M. B. Hinman, G. P. Holland, J. L. Yarger, R. V. Lewis, Inducing β-sheets formation in synthetic spider silk fibers by aqueous post-spin stretching. *Biomacromolecules* **12**, 2375–2381 (2011).
50. P. C. Chung, E. Glynos, P. F. Green, The elastic mechanical response of supported thin polymer films. *Langmuir* **30**, 15200–15205 (2014).
51. W. Xia, S. Keten, Interfacial stiffening of polymer thin films under nanoconfinement. *Extreme Mech. Lett.* **4**, 89–95 (2015).
52. W. Xia, J. Song, D. D. Hsu, S. Keten, Understanding the interfacial mechanical response of nanoscale polymer thin films via nanoindentation. *Macromolecules* **49**, 3810–3817 (2016).
53. A. Giuntoli, S. Keten, Tuning star architecture to control mechanical properties and impact resistance of polymer thin films. *Cell Rep. Phys. Sci.* **2**, 100596 (2021).
54. W. Xia, J. Song, C. Jeong, D. D. Hsu, F. R. Phelan Jr., J. F. Douglas, S. Keten, Energy-renormalization for achieving temperature transferable coarse-graining of polymer dynamics. *Macromolecules* **50**, 8787–8796 (2017).
55. S. V. Subramani, J. Li, K. Z. Lee, N. Fisher, F. Zhang, Blending recombinant amyloid silk proteins generates composite fibers with tunable mechanical properties. *Mater. Adv.* **5**, 3506–3516 (2024).
56. B. Dai, C. J. Sargent, X. Gui, C. Liu, F. Zhang, Fibril self-assembly of amyloid-spider silk block polypeptides. *Biomacromolecules* **20**, 2015–2023 (2019).
57. T. Lefèvre, F. Paquet-Mercier, J. F. Rioux-Dubé, M. Pézolet, Review: Structure of silk by Raman spectromicroscopy: From the spinning glands to the fibers. *Biopolymers* **97**, 322–336 (2012).
58. Y. Hsia, E. Gnesa, R. Pacheco, K. Kohler, F. Jeffery, C. Vierra, Synthetic spider silk production on a laboratory scale. *J. Vis. Exp.* e4191 (2012).
59. A. Lazaris, S. Arcidiacono, Y. Huang, J. F. Zhou, F. Duguay, N. Chretien, E. A. Welsh, J. W. Soares, C. N. Karatzas, Spider silk fibers spun from soluble recombinant silk produced in mammalian cells. *Science* **295**, 472–476 (2002).
60. S. Keten, M. J. Buehler, Nanostructure and molecular mechanics of spider dragline silk protein assemblies. *J. R. Soc. Interface* **7**, 1709–1721 (2010).
61. S. Keten, Z. Xu, B. Ihle, M. J. Buehler, Nanoconfinement controls stiffness, strength and mechanical toughness of β-sheet crystals in silk. *Nat. Mater.* **9**, 359–367 (2010).
62. S. Keten, M. J. Buehler, Atomistic model of the spider silk nanostructure. *Appl. Phys. Lett.* **96**, 153701 (2010).
63. T. Giesa, C. C. Perry, M. J. Buehler, Secondary structure transition and critical stress for a model of spider silk assembly. *Biomacromolecules* **17**, 427–436 (2016).
64. W. Shen, Z. Tang, X. Wu, L. Pan, Y. Cheng, B. Huo, J. Song, W. Chen, B. Ji, D. Li, An atomistic model of silk protein network for studying the effect of pre-stretching on the mechanical performances of silks. *Acta Mech. Sin.* **38**, 222013 (2022).
65. W. Xia, J. Song, N. K. Hansoge, F. R. Phelan Jr., S. Keten, J. F. Douglas, Energy renormalization for coarse-graining the dynamics of a model glass-forming liquid. *J. Phys. Chem. B* **122**, 2040–2045 (2018).
66. J. Song, D. D. Hsu, K. R. Shull, F. R. Phelan Jr., J. F. Douglas, W. Xia, S. Keten, Energy renormalization method for the coarse-graining of polymer viscoelasticity. *Macromolecules* **51**, 3818–3827 (2018).
67. T. Arndt, P. R. Laity, J. Johansson, C. Holland, A. Rising, Native-like flow properties of an artificial spider silk dope. *ACS Biomater. Sci. Eng.* **7**, 462–471 (2021).
68. M.-Y. Wang, J.-P. Zhang, S.-L. Chen, B. Qi, X.-Y. Yao, X.-H. Zhang, Y.-T. Li, Z.-H. Yang, Dry-spinning of artificial spider silk ribbons from regenerated natural spidroin in an organic medium. *Macromol. Rapid Commun.* **44**, e2300024 (2023).
69. M. Boulet-Audet, C. Holland, T. Gheysens, F. Vollrath, Dry-spun silk produces native-like fibroin solutions. *Biomacromolecules* **17**, 3198–3204 (2016).
70. X. Chen, Z. Shao, F. Vollrath, The spinning processes for spider silk. *Soft Matter* **2**, 448–451 (2006).
71. A. P. Thompson, H. M. Aktulga, R. Berger, D. S. Bolintineanu, W. M. Brown, P. S. Crozier, P. J. in 't Veld, A. Kohlmeyer, S. G. Moore, T. D. Nguyen, R. Shan, M. J. Stevens, J. Tranchida, C. Trott, S. J. Plimpton, LAMMPS - A flexible simulation tool for particle-based materials modeling at the atomic, meso, and continuum scales. *Comput. Phys. Commun.* **271**, 108171 (2022).
72. R. J. Gowers, M. Linke, J. Barnoud, T. J. E. Reddy, M. N. Melo, S. L. Seyler, J. Domanski, D. L. Dotson, S. Buchoux, I. M. Kenney, O. Beckstein, "MDAnalysis: A Python package for the rapid analysis of molecular dynamics simulations," in *Proceedings of the 15th Python in Science Conference* (SciPy, 2019); www.osti.gov/biblio/1565806.
73. N. Michaud-Agrawal, E. J. Denning, T. B. Woolf, O. Beckstein, MDAnalysis: A toolkit for the analysis of molecular dynamics simulations. *J. Comput. Chem.* **32**, 2319–2327 (2011).
74. V. Calandrini, E. Pellegrini, P. Calligari, K. Hinsen, G. R. Kneller, nMoldyn - Interfacing spectroscopic experiments, molecular dynamics simulations and models for time correlation functions. *SFN Collect.* **12**, 201–232 (2011).
75. P. de Buyl, tidynamics: A tiny package to compute the dynamics of stochastic and molecular simulations. *J. Open Source Softw.* **3**, 877 (2018).
76. M. Wojdyr, Fityk: A general-purpose peak fitting program. *J. Appl. Cryst.* **43**, 1126–1128 (2010).
77. R. D. Groot, K. L. Rabone, Mesoscopic simulation of cell membrane damage, morphology change and rupture by nonionic surfactants. *Biophys. J.* **81**, 725–736 (2001).
78. R. D. Groot, P. B. Warren, Dissipative particle dynamics: Bridging the gap between atomistic and mesoscopic simulation. *J. Chem. Phys.* **107**, 4423–4435 (1997).
79. J. Y. Wong, J. McDonald, M. Taylor-Pinney, D. I. Spivak, D. L. Kaplan, M. J. Buehler, Materials by design: Merging proteins and music. *Nano Today* **7**, 488–495 (2012).
80. A. Maiti, S. McGrother, Bead-bead interaction parameters in dissipative particle dynamics: Relation to bead-size, solubility parameter, and surface tension. *J. Chem. Phys.* **120**, 1594–1601 (2004).
81. D. Porter, *Group Interaction Modelling of Polymer Properties* (CRC Press, 1995).

Acknowledgments: We acknowledge support from the computational resources and staff contributions provided for the Quest high-performance computing facility at Northwestern University, which is jointly supported by the Office of the Provost, the Office for Research, and Northwestern University Information Technology. We also acknowledge A. Pandey for providing the data on the effect of *B*-factor on spider silk mechanical properties based on a previously developed machine learning model. **Funding:** This work was supported by the National Science Foundation (OIA-2219142 to F.Z. and S.K. and DMR-2207879 to F.Z.). J.J.G. was also supported by the NSF Graduate Research Fellowship (grant no. DGE-1842165) and the Ryan Fellowship organized through the International Institute for Nanotechnology at Northwestern University. **Author contributions:** Conceptualization: J.J.G., S.V.S., X.Y., F.Z., and S.K. Methodology: J.J.G., S.V.S., X.Y., and T.M.R. Software: J.J.G., X.Y., and T.M.R. Validation: J.J.G., X.Y., S.V.S., and T.M.R. Investigation: J.J.G., S.V.S., X.Y., and T.M.R. Visualization: J.J.G. and S.V.S. Supervision: J.J.G., F.Z., and S.K. Writing—original draft: J.J.G. and S.V.S. Writing—review and editing: J.J.G., S.V.S., X.Y., T.M.R., F.Z., and S.K. Funding acquisition: J.J.G., F.Z., and S.K. **Competing interests:** The authors declare that they have no competing interests. **Data and materials availability:** All data needed to evaluate the conclusions in the paper are present in the paper and/or the Supplementary Materials. A GitHub repository was published using Zenodo (https://doi.org/10.5281/zenodo.14041545) containing instructions for setting up simulations using this modeling framework. The version published along this paper can also be accessed directly from GitHub at (https://github.com/keten-group/DPD-Silk-Analysis-Package/releases/tag/v1.0.1).

Submitted 2 July 2024
Accepted 3 February 2025
Published 7 March 2025
10.1126/sciadv.adr3833